CTU Journal of Innovation and Sustainable Development
ISSN 2588-1418 | e-ISSN 2815-6412

DOI:10.22144/ctujoisd.2025.052

Non-destructive detection of ovary regions in live female mud crabs by machine-learning assisted multispectral imaging

Hai-Dang Vo[1,2], Nhut-Thanh Tran[3], and Masayuki Fukuzawa[1*]

[1]*Graduate School of Science and Technology, Kyoto Institute of Technology, Japan*

[2]*Faculty of Multimedia Communications, College of Information and Communication Technology, Can Tho University, Viet Nam*

[3]*Faculty of Automation Engineering, College of Engineering, Can Tho University, Viet Nam*

**Corresponding author (fukuzawa@kit.ac.jp)*

Article info.

Received 14 Jul 2025
Revised 18 Aug 2025
Accepted 28 Sep 2025

Keywords

Automatic mud crab grading, in vivo condition, multispectral imaging, ovary region, spectrometric features

ABSTRACT

Ovarian fullness of female mud crabs (Scylla paramamosain) is key determinant of market value but is still assessed subjectively by hand. Spectrometry offers an objective alternative, and our previous studies under in vitro and semi-in vivo conditions demonstrated the potential of spectrometric features for discrimination of crab tissues (meat, ovary, hepatopancreas, and shell). However, it was still challenging to apply under in vivo conditions. This study aims to detect the ovary region in live mud crabs while keeping the 'in vivo' condition by combining a custom multispectral-imaging system and simple ML techniques. A special optical setup and a concise multispectral camera were included in the system aiming to acquire the transmission image through the intact carapace practically in the crab-farming fields. The ovary region was predicted pixel-wise and patch-wise using conventional classifiers (Logistic Regression, Random Forest, Gradient Boosting, k-NN, and SVM) and Convolutional Neural Networks (CNN), enhanced by Principal Component Analysis (PCA) for feature transformation. The patch-wise random forest model with PCA (7×7 patches) achieved superior performance, with an accuracy of 0.872 and an F1-score of 0.872, outperforming other methods. These findings mark a significant advancement in the application of multispectral imaging for automated, non-destructive quality assessment in live aquaculture specimens.

1. INTRODUCTION

Scylla paramamosain, commonly known as the mud crab, is a crustacean of significant economic value, widely cultivated and harvested across numerous regions globally (Keenan et al., 1998; Shelley & Lovatelli, 2011; Bhuiyan et al., 2021). Within the supply chain—from farmers to collectors and exporters, mud crabs are graded and traded based on quality assessments that consider both external traits (e.g., body weight, size, and appendage condition) and internal criteria. For female crabs, ovarian fullness is the most critical internal factor determining economic value, while meat yield is a key criterion for male crabs (C-AID Consultants, 2016).

Assessing internal attributes such as ovarian fullness poses a notable challenge, as external quality traits can be evaluated through visual inspection or weighing, whereas current methods rely on indirect, manual techniques. These include palpating the

carapace for firmness or inspecting the crab's carapace under strong light, which are highly subjective and often yield inconsistent results among assessors (C-AID Consultants, 2016). This has driven a growing demand for objective, reproducible, and non-invasive approaches to internal quality evaluation in mud crabs.

Numerous studies have advanced our understanding of the biological, biochemical, and morphological dynamics of the ovary, hepatopancreas, and muscle tissues in Scylla paramamosain under varying environmental and physiological conditions (Aaqillah-Amr et al., 2018; Wu et al., 2019; Amin-Safwan et al., 2019; Wu et al., 2020; Han et al., 2024; Fang et al., 2025; Jiang et al., 2025; Yu et al., 2025). However, these investigations predominantly depend on invasive sampling and laboratory-based biochemical analyses, limiting their applicability in live settings.

The spectrometric technique is one of the promising tools for non-destructive internal quality assessment. There were several attempts to integrate machine learning (ML) methods with multispectral and hyperspectral imaging (MSI/HSI) for non-destructive quality evaluation in various aquatic products. In fish, shrimp, and other seafood, ML models—ranging from partial least squares regression to convolutional neural networks—combined with MSI/HSI have accurately predicted freshness, chemical composition, and adulteration (Moosavi-Nasab et al., 2021; Kong et al., 2022; Li et al., 2023; Shao et al., 2023; Zhang et al., 2020; Ismail et al., 2023). For example, Wold et al. (2024) developed a rapid, non-invasive method using near-infrared spectroscopy and ML to quantify meat content in live red king crab legs, achieving high accuracy (R^2 = 0.83–0.90, RMSEP = 6.1–6.2%) depending on the specific trial and validation set. These advancements underscore the potential of spectral imaging and ML for internal quality assessment in live crustaceans. Despite these progressions, robust, real-time solutions for non-destructive ovary detection in live Scylla paramamosain remain elusive due to the crab's complex internal structure, crab morphology, and lack of annotated datasets or spectral characteristics.

Towards automatic internal quality grading of mud crabs, our research group has been focused on a practical technique of ML-assisted spectrometry by strategically iterative prototyping of various spectrometric systems for in-vitro, semi-in vivo and in vivo conditions (Tran et al., 2024). Initial in-vitro studies have shown potential in differentiating internal components (e.g., meat, ovary, hepatopancreas, and shell) in mud crabs, with principal component analysis (PCA) and machine learning to yield encouraging classification results (Tran et al., 2024; Vo et al., 2025). However, the in-vitro studies required destructive sampling or were impractical for large-scale, in vivo applications, remaining a critical gap in scalable and efficient internal organ detection.

This study aims to detect ovary region in live mud crabs while keeping 'in vivo' condition by combining a custom multispectral-imaging system and simple ML techniques. The system includes a special optical setup and a concise multispectral camera to acquire the transmission image through the intact carapace practically in the crab-farming fields. The ML techniques to be examined include patch-wise classification with Random Forest and CNN models.

The remainder of this paper is as follows: Section 2 describes the materials and methods, including sample preparation, the design of the custom multispectral imaging system, data acquisition, and preprocessing steps. Section 3 presents the results and discussion, evaluating the feasibility of the proposed ovary region detection framework. Finally, section 4 concludes with a summary of key findings and proposes directions for future research.

2. METHOD

2.1. Sample preparation

Fifty female mud crabs (Scylla paramamosain) were sourced from commercial aquaculture ponds in Bac Lieu province, Mekong Delta, Viet Nam during June–July 2025. Experienced farmers selected the crabs to ensure a high-quality, representative sample, using visual assessment of external features to capture a diverse range of maturity stages. After collection, crabs were promptly transported to the laboratory under controlled conditions to maintain stable conditions and minimize physiological changes. Upon arrival, each crab was individually weighed and measured to record key physical characteristics, including body weight, carapace width, and carapace length (Figure 1a). The crabs exhibited a mean carapace width of 106.6 mm (range: 96.0–115.0 mm), a mean carapace length of 79.0 mm (range: 70.0–85.0 mm), and a mean body weight of 229.2 g (range: 160.0–285.0).

Each crab was first imaged with the intact carapace under 'in vivo' conditions. Subsequently, the crabs

were euthanized, and their carapaces were carefully removed to expose internal organs, particularly the ovary (Figure 1b). This step enabled precise identification and annotation of the ovary region, serving as the ground truth for model development.

It should be noted that this destructive step was performed solely to obtain ground-truth annotations of the ovary region. This procedure was necessary only during dataset preparation and annotation, while all multispectral imaging of intact crabs was conducted under in vivo conditions. Thus, the imaging methodology itself remains entirely non-destructive.

Additionally, the ovaries were extracted and weighed, providing quantitative data for further analysis and validation. All sample preparation steps, including physical measurements, ovary extraction, and imaging, followed a standardized workflow to ensure reproducibility and minimize variability across the dataset.

Figure 1. (a) Physical measurement of carapace and body weight; (b) Carapace removal for ovary annotation

2.2. A custom multispectral imaging system

A custom multispectral imaging system was developed for live mud crabs, optimized to capture internal organ characteristics, particularly the ovary, through the carapace (Figure 2). The system comprises three main components: (1) halogen bulbs as the illumination source, (2) collimating optics, and (3) an imaging unit, designed for high-quality, non-invasive imaging.

The illumination source consists of two parallel lines of halogen bulbs delivering uniform, collimated light through the crab sample. The first line (L1) comprised three halogen bulbs arranged as 50 W–100 W–50 W (12VDC), while the second line (L2) used a single 100 W (12VDC) bulb positioned opposite L1. This arrangement illuminated the crab from both sides, with L1 targeting the crab's mouth and L2 illuminating the rear, ensuring full carapace coverage. Each line was equipped with optical components: light from the bulbs passed through two Fresnel lens bars (focal length: 12 mm; size: 200 mm × 35 mm) and a cylindrical plano-convex lens (focal length: 23.9 mm; size: 200 mm × 31 mm). This setup produced a collimated, line-shaped beam (approximately 200 mm long and 10 mm wide), selectively illuminating the target region of the crab to minimize stray light and enhance signal clarity. The distance between the cylindrical lenses of the two lines was set to approximately 190 mm for optimal alignment and light transmission.

To ensure consistent positioning and registration of the crab during imaging, a custom sample holder was used to maintain the crab in a fixed orientation, enabling repeatable imaging with and without the carapace. A shield plate with an oval cutout was placed between the camera and sample to allow only the carapace to be illuminated and captured. Additional light shields and a dark slide eliminated ambient light, ensuring a controlled imaging environment.

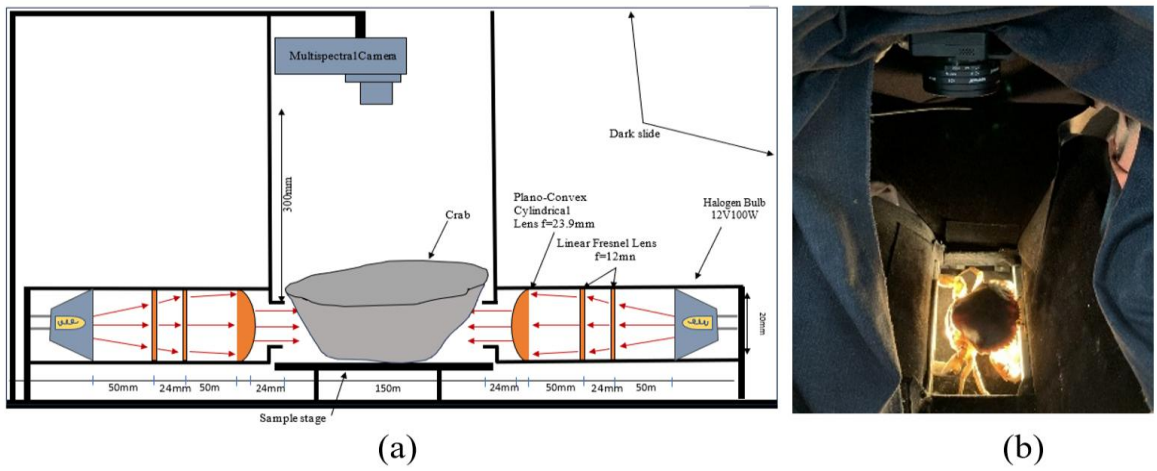

Figure 2. Multispectral imaging setup: (a) schematic of the optical setup; (b) practical implementation

A commercial multispectral camera (MONARCH II EVK UNS54000) was mounted vertically above the sample, equipped with an f/4.7 aperture lens (effective focal length: 4.98 mm). It provided a field of view of 31.5° (horizontal) and 25.5° (vertical), capturing images at 1280 × 1024 pixels. Spectral imaging spanned ten bands centered at 713, 736, 759, 782, 805, 828, 851, 874, 897, and 920 nm. The lens-to-sample distance was fixed at 300.0 mm for consistent imaging geometry.

Multispectral images were acquired at four exposure times (167, 200, 250, and 500 ms) to account for varying tissue density and light penetration. Reference RGB images, captured using an 8 MP CMOS camera, shared identical fields of view to facilitate downstream analysis and mask transfer.

2.3. Data acquisition

Multispectral and reference images were acquired for each crab following a standardized protocol with fixed camera positioning and consistent lighting to ensure data quality. Initially, the live crab was positioned in the optical setup to maintain uniform orientation and field of view. Multispectral images of the crab with the intact carapace were acquired at four exposure times (167, 200, 250, and 500 ms) to account for varying tissue density and light transmission properties. The camera position and imaging geometry remained constant across all samples.

After initial imaging, the crab was euthanized, and the carapace was precisely removed to expose internal tissues, particularly the ovary. The crab, now without the carapace, was repositioned in the same setup, and a second set of multispectral images was captured using identical parameters and fields of view. Concurrently, an RGB camera captured reference images with and without the carapace to aid annotators in delineating the ovary region in multispectral images.

To enable spectral normalization and account for light source variations, a reference spectrum was obtained for each imaging batch using a 45° stainless steel mirror, chosen for its uniform reflectance properties, under the same illumination conditions as the crab samples.

2.4. Data preprocessing

Carapace segmentation was done using Otsu's thresholding method to create an initial binary mask for each carapace. It is noted that the pixels near the carapace edge are inevitably saturated even under a proper exposure for the carapace inside because of their significant thickness decreases. In order to relieve the risk of those saturated pixels compromising the spectrometric accuracy, the carapace mask was reduced by 10% prior to further analysis. This shrinkage rate was determined based on data showing its effectiveness in minimizing edge saturation while retaining sufficient data coverage. Specifically, as shrinkage increased from 0% to 30%, the mean intensity and variability of normalized spectral values at 713 nm decreased, with values dropping from a mean of 0.41 at 0% to 0.18 at 30%. The rate of reduction stabilized beyond 10% (mean: 0.2992, 25th percentile: 0.0943, 75th percentile: 0.3558), indicating that further shrinkage yielded diminishing returns. As shown in Figure 3, this 10% reduction effectively excluded saturated edge pixels while preserving data integrity.

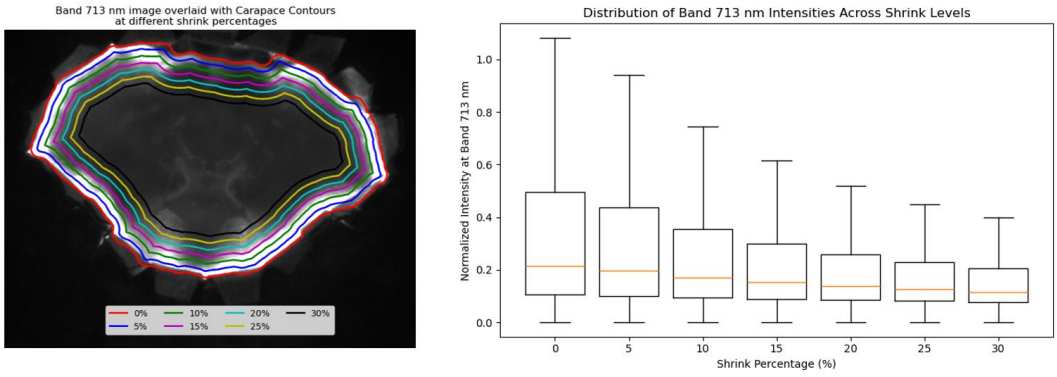

(a) (b)

Figure 3. (a) An example image of 712 nm band with carapace region contours and (b) box plot of normalized pixel values inside the carapace region, under different shrinkage rates

Spectral data were then screened to remove images with excessive pixel saturation. Pixel-level saturation was assessed for each spectral band by calculating the maximum intensity, I_{max}, and the saturation threshold T as:

$$T = 0.99 I_{max} \quad (1)$$

Pixels with intensity $I(x, y) > T$ were classified saturated, and the fraction of saturated pixels, f_{sat}, was computed as:

$$f_{sat} = \frac{N_{sat}}{N_{tot}} \quad (2)$$

Where N_{sat} and N_{tot} denote the number of saturated pixels and the total pixels within the carapace, respectively. Images with $f_{sat} > 10\%$ in any band were excluded as outliers.

The retained spectral data were normalized band-wise using the reference spectrum from each imaging batch, as described in Section 2.3, according to:

$$\hat{C}(x, y, b) = \frac{C(x,y,b)}{R(b)} \quad (3)$$

where $\mathrm{C(x, y, b)}$ is the raw intensity at pixel (x, y) in band b, $\mathrm{R(b)}$ is the reference-spectra value for band b, and $\hat{C}(\mathrm{x}, \mathrm{y}, \mathrm{b})$ is the normalized interactance spectrum.

After screening, the dataset was reduced to 31 multispectral images, each with 10 spectral bands, totaling nearly 9 million pixels within the segmented carapace regions. Two classification strategies—pixel-wise and patch-wise—were employed, benchmarked using Logistic Regression, Random Forest, Gradient Boosting, k-Nearest Neighbors (k-NN), Support Vector Machine (SVM), and Convolutional Neural Network (CNN) models.

Model hyperparameters were tuned through grid search combined with cross-validation within the training folds. For example, the number of trees and maximum depth in Random Forest, the learning rate in Gradient Boosting, and the number of neighbors in k-NN were systematically optimized. SVM hyperparameters (kernel type and regularization parameter C) were selected based on validation performance. For CNNs, hyperparameters such as patch size, learning rate, and batch size were empirically adjusted. The final reported results correspond to the best-performing configurations.

The class distribution was moderately imbalanced, with ovary pixels comprising 43% and non-ovary pixels 57% of the dataset.

For patch-wise classification, each carapace was divided into non-overlapping square patches of side length p with $p \times p$ pixels across all b spectral bands flattened into a single feature vector of length $p^2 \times$ b. Non-overlapping patches were used to reduce computational complexity while preserving spatial context. Patches were labeled positive (1) if more than half their pixels overlapped with the ovary mask, and negative (0) otherwise. Feature vectors and labels were compiled into a data matrix $\mathbf{X} \in R^{N \times (p^2 \times \mathrm{b})}$, containing (N) flattened patch samples, paired with a binary label vector $\mathbf{y} \in \{0,1\}^N$.

Ovary regions were annotated as described in Section 2.3, using a two-step process for accurate and reproducible ground truth labeling (Figure 5). Initially, manual annotation was performed on "no-carapace" images of crabs after carapace removal,

where the ovary and other internal tissues were clearly visible. However, as multispectral images extend beyond the visible spectrum, directly annotating the ovary region in these images poses challenges. To address this, an RGB reference image of each crab, captured with the same field of view, was provided to guide annotators in accurately delineating ovary boundaries.

In the second step, the manually annotated ovary mask was spatially aligned and transferred to the corresponding multispectral images of the same crab with the carapace intact. During this process, annotators carefully adjusted the mask's position and orientation using visible anatomical landmarks and reference axes to ensure precise registration without altering its shape. This streamlined workflow facilitated reliable and reproducible generation of ovary ground truth labels for subsequent model training and evaluation.

Given the limited dataset size, model performance was evaluated using 10-fold cross-validation. The data were randomly divided into ten folds; in each iteration, nine folds were used for training and one for testing. Reported metrics represent the average across all folds.

Figure 4 presents a comprehensive overview of the experimental and analytical pipeline implemented in this study, illustrating the integrated workflow from sample preparation to data analysis.

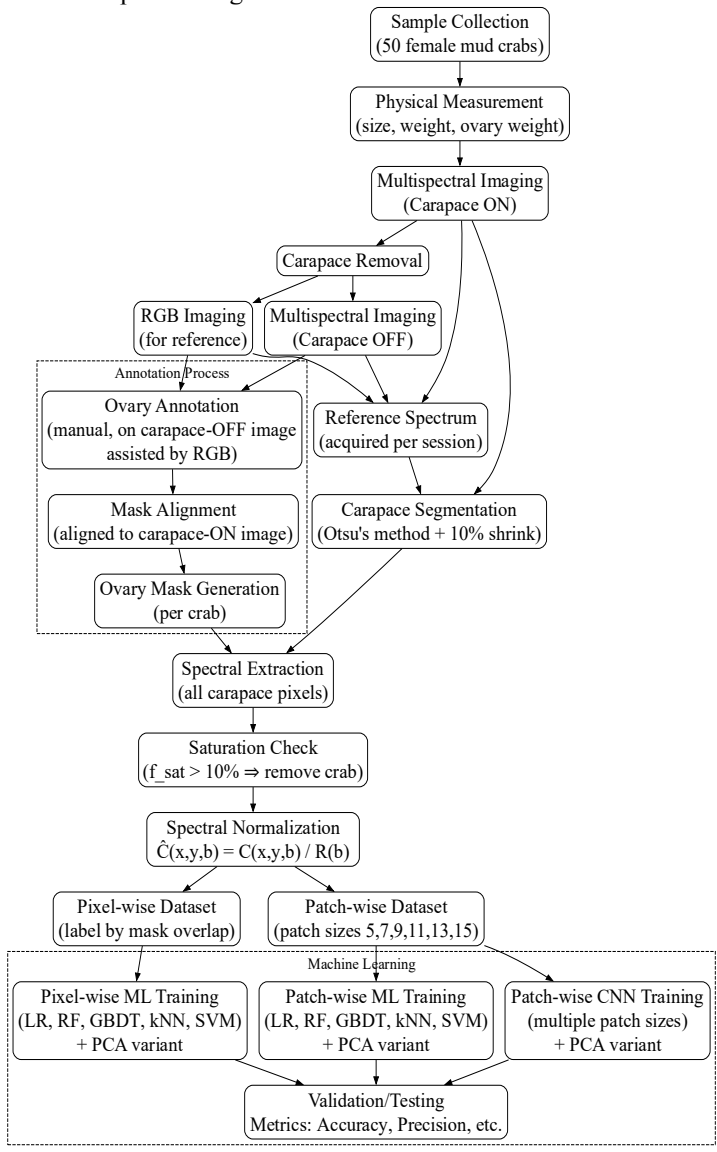

Figure 4. Pipeline of ovary detection in mud crabs using multispectral imaging

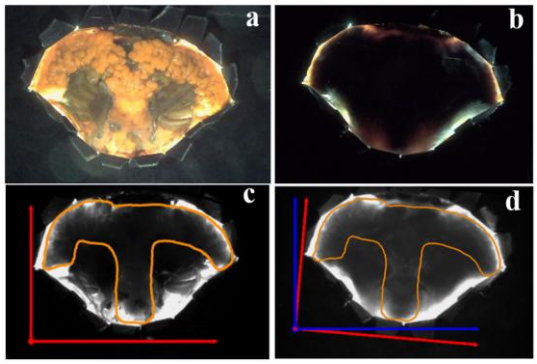

Figure 5. Typical images used in ovary annotation and mask transfer: (a) RGB no-carapace image; (b) RGB image with intact carapace; (c) multispectral no-carapace image with annotated ovary boundary; (d) annotated mask transferred to multispectral image with intact carapace

3. RESULTS AND DISCUSSION

The performance of the proposed multispectral imaging pipeline for non-destructive ovary detection in mud crabs was assessed through comprehensive quantitative and qualitative analyzes.

To explore the spectral characteristics and variability of each tissue type supporting ovary detection, Figure 6 shows the mean normalized interactance spectra (±1 SD) for carapace and ovary regions across all measured wavelengths. The ovary consistently displayed lower interactance values than the carapace, particularly in longer wavelength bands (≥828 nm). This distinct spectral separation between tissues confirms the suitability of multispectral data for internal organ detection.

Classification performance for various machine learning models, using pixel-wise and patch-wise approaches with and without Principal Component Analysis (PCA), is summarized in Tables 1 and 2. For pixel-wise classification (Table 1), the Random Forest classifier achieved the highest performance, with an accuracy of 0.7460 and an F1-score of 0.7455, outperforming Logistic Regression, Gradient Boosting, SVM, and k-Nearest Neighbors (k-NN). PCA had minimal impact on pixel-wise results.

In contrast, patch-wise classification (Table 2), using a 7×7 patch size selected for its balance of spatial context and computational efficiency, showed significant improvements. Without PCA, k-NN achieved the highest accuracy and F1-score (0.8292), closely followed by Random Forest. With PCA, applied to reorient the feature space while retaining all components to preserve full spectral information and enhance classifier separability, Random Forest emerged as the top performer, achieving an accuracy of 0.8723 and an F1-score of 0.8722—the best among all tested configurations.

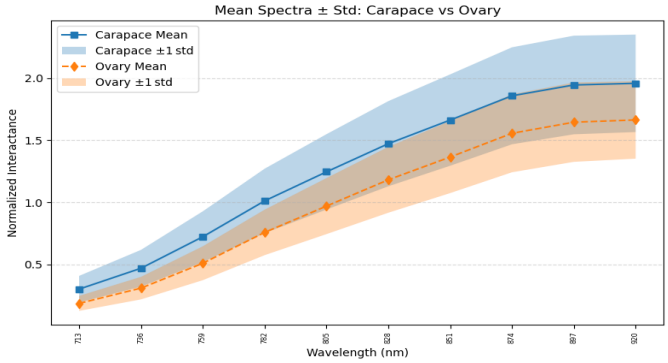

Figure 6. Mean normalized interactance spectra (± σ) for carapace (light-blue, 10% shrunk mask) and ovary (light-orange) regions across all wavelengths

Table 1. Pixel-wise Classification Performance (with and without PCA)

Model	No PCA				With PCA			
	Accuracy	Precision	Recall	F_1-Score	Accuracy	Precision	Recall	F_1-Score
Logistic Regression	0.687	0.704	0.684	0.679	0.687	0.704	0.684	0.679
Random Forest	0.746	0.747	0.746	0.746	0.744	0.744	0.743	0.743
Gradient Boosting	0.709	0.711	0.708	0.707	0.720	0.722	0.719	0.718
K-NN (n=9)	0.729	0.729	0.728	0.728	0.695	0.697	0.693	0.693
SVM	0.684	0.706	0.681	0.673	0.684	0.706	0.681	0.6731

Further enhancements were explored using convolutional neural networks (CNNs) in a patch-wise framework. As shown in Tables 3, without PCA, the CNN achieved optimal performance at a patch size of 15 (accuracy 0.8052, F1-score 0.8048). With PCA, the best performance occurred at a patch size of 9 (accuracy and F1-score of 0.8401), indicating that deep learning, combined with appropriate patch sizing and feature transformation, delivers competitive results.

Figure 7 compares ground truth ovary masks (yellow) with predictions (red) from Random Forest and CNN models (both with PCA) for two representative crabs (A1 and A4). Random Forest predictions, leveraging the 7×7 patch size, more closely aligned with ground truth boundaries compared to CNN predictions at a 9×9 patch size, reflecting Random Forest's superior quantitative performance. Both patch-wise approaches produced smoother, more cohesive predictions than pixel-wise methods, demonstrating the practical effectiveness of the classification pipeline. Notably, the CNN models showed weaker performance than Random Forest. This is likely due to the limited dataset size, as CNNs generally require large amounts of data to learn complex spectral–spatial features effectively, whereas tree-based models such as Random Forest are more robust with smaller datasets. With a larger annotated dataset, CNN performance may be expected to improve.

This study introduced multispectral imaging for non-destructive ovary region detection in female mud crabs under 'in vivo' conditions, using a custom multispectral imaging system to capture spectral characteristics of ovary regions through the intact carapace. Patch-wise classification, particularly with PCA and Random Forest models, outperformed both pixel-wise methods and CNN-based patch-wise approaches, achieving high accuracy and F1-scores by leveraging spatial and spectral features. A dual-modality annotation strategy, using RGB reference images aligned with multispectral data, ensured accurate and reproducible ovary labeling. This study showed a novel approach by applying CNN-based patch-wise classification for ovary detection in mud crabs, with PCA enhancing feature separability without dimensionality reduction.

Limitations include a small annotated dataset, which may limit model generalizability, necessitating larger datasets. The present version of the multispectral imaging system, optimized for controlled conditions, may face challenges from environmental variability or crab morphology in real-world settings. Despite these limitations, the findings in this study demonstrated the feasibility of spectral-based, non-destructive ovary detection, laying a foundation for automated systems in aquaculture and quality assessment.

Table 2. Patch-wise Classification Performance (7×7 patch, with and without PCA)

Model	No PCA				With PCA			
	Accuracy	Precision	Recall	F_1-Score	Accuracy	Precision	Recall	F_1-Score
Logistic Regression	0.709	0.723	0.708	0.703	0.697	0.715	0.695	0.689
Random Forest	0.790	0.793	0.790	0.790	0.872	0.873	0.872	0.872
Gradient Boosting	0.724	0.727	0.724	0.723	0.762	0.764	0.761	0.761
K-NN (n=9)	0.829	0.829	0.829	0.829	0.851	0.852	0.851	0.851
SVM	0.741	0.748	0.740	0.739	0.790	0.797	0.789	0.788

Table 3. CNN Patch-wise Performance (by Patch Size, with and without PCA)

Patch Size	No PCA				With PCA			
	Accuracy	Precision	Recall	F_1-Score	Accuracy	Precision	Recall	F_1-Score
7	0.792	0.794	0.791	0.791	0.829	0.830	0.829	0.829
9	0.802	0.803	0.802	0.802	0.840	0.840	0.840	0.840
11	0.803	0.804	0.803	0.803	0.823	0.825	0.823	0.823
13	0.792	0.793	0.792	0.792	0.816	0.817	0.816	0.816
15	0.805	0.807	0.805	0.805	0.801	0.802	0.801	0.801

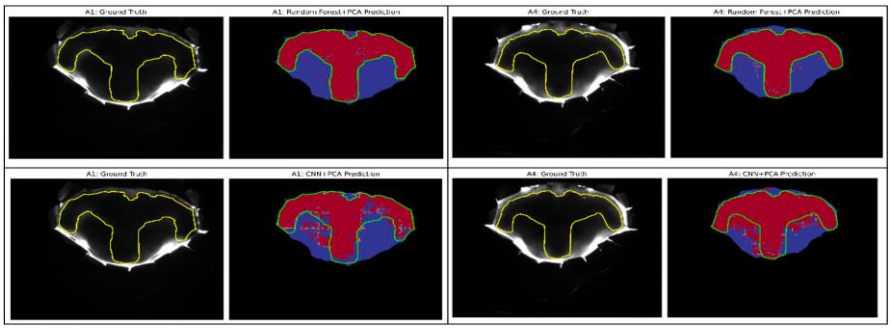

Figure 7. Comparison of ground truth ovary masks (yellow) and predicted ovary regions (red) for representative two crabs (A1 and A4) using RF (first row) and CNN (second row) models with PCA

4. CONCLUSION

This study demonstrated the efficacy of multispectral imaging for non-destructive ovary detection in female mud crabs (Scylla paramamosain) under 'in vivo' conditions, utilizing a multispectral imaging system to capture spectral characteristics of ovary regions through the intact carapace. The integration of pixel-wise and patch-wise classification pipelines, benchmarked across traditional machine learning models (Logistic Regression, Random Forest, Gradient Boosting, k-NN, SVM) and CNNs, revealed that patch-wise approaches, particularly Random Forest with PCA transformation (7×7 patch size), achieved the highest performance (accuracy: 0.8723, F1-score: 0.8722), surpassing pixel-wise methods and CNN-based patch-wise models (best at 9×9 patch size with PCA, accuracy: 0.8401). PCA, applied as a feature transformation to enhance separability while retaining all components significantly improved patch-wise classification outcomes.

This study is the first to apply CNN-based patch-wise classification for ovary detection in mud crabs under 'in vivo' conditions, highlighting the potential of deep learning to capture subtle spectral and spatial features. These findings provide a robust foundation for spectral-based, automated internal quality grading of mud crabs, with significant potential to revolutionize aquaculture practices. By enabling non-destructive assessment of critical attributes such as ovarian fullness, this approach will offer a more efficient and objective solution for quality control in the aquaculture industry.

Despite these advancements, limitations include the small dataset, which may limit model generalizability, and the challenges of complex internal structures and environmental variability or crab morphology, which affect detection consistency in real-world settings. These factors hinder the scalability of the proposed method. Future research should aim to develop larger and more diverse datasets to improve model robustness, further optimize optical systems for practical deployment, and create scalable solutions for comprehensive quality grading in real-world aquaculture settings.

CONFLICT OF INTEREST

The authors have no competing interests to declare that are relevant to the content of this article.

ACKNOWLEDGMENT

This work was supported by JST SPRING, Grant Number JPMJSP2107 and by JSPS Core-to-Core Program, Grant Number JPJSCCB20230005.

REFERENCES

Keenan, C. P., Davie, P. J. F., & Mann, D. L. (1998). A revision of the genus *Scylla* de Haan, 1833 (Crustacea: Decapoda: Brachyura: Portunidae). *The Raffles Bulletin of Zoology, 46*(1), 217–245.

Shelley, C., & Lovatelli, A. (2011). *Mud crab aquaculture: A practical manual (FAO Fisheries and Aquaculture Technical Paper No. 567).* Food and Agriculture Organization of the United Nations. http://www.fao.org/3/ba0110e/ba0110e.pdf

Bhuiyan, M. S., Shamsuzzaman, M. M., Hossain, M. M., Mitu, S. J., & Mozumder, M. M. H. (2021). Mud crab (*Scylla serrata* Forsskål, 1775) value chain analysis in the Khulna region of Bangladesh. *Aquaculture and Fisheries, 6*(3), 330–336. https://doi.org/10.1016/j.aaf.2021.01.004

C-AID Consultants. (2016). *Australian industry live mud crab grading scheme* (Version 3) [PDF]. Retrieved from https://www.c-aid.com.au/wp-

content/uploads/Mud-Crab-Grading-Scheme-V3-2016.pdf

Wu, Q., Waiho, K., Huang, Z., Li, S., Zheng, H., Zhang, Y., Ikhwanuddin, M., Lin, F., & Ma, H. (2020). Growth performance and biochemical composition dynamics of ovary, hepatopancreas and muscle tissues at different ovarian maturation stages of female mud crab, *Scylla paramamosain*. *Aquaculture, 515*, 734560. https://doi.org/10.1016/j.aquaculture.2019.734560

Fang, K., Wu, K., Wang, J., Liu, G., Ouyang, W., Lin, G., Tian, H., Feng, M., & Wen, X. (2025). Comparative analysis of fatty acid, amino acid, and mineral of wild female mud crabs (*Scylla paramamosain*) from the southeast coast of China: Insights for consumer preference. *Journal of Food Composition and Analysis, 145*, 107808. https://doi.org/10.1016/j.jfca.2025.107808

Jiang, X., Wang, W., Liu, M., Lin, Z., & Zheng, X. (2025). Comparative analysis of morphological characteristics and nutritional quality in wild-caught and pond-reared female mud crab, *Scylla paramamosain*. *Journal of Food Composition and Analysis, 146,* 107953. https://doi.org/10.1016/j.jfca.2025.107953

Wu, Q., Shi, X., Fang, S., Xie, Z., Guan, M., Li, S., Zheng, H., Zhang, Y., Ikhwanuddin, M., & Ma, H. (2019). Different biochemical composition and nutritional value attribute to salinity and rearing period in male and female mud crab *Scylla paramamosain***.** *Aquaculture*, *513*, 734417. https://doi.org/10.1016/j.aquaculture.2019.734417

Amin-Safwan, A., Mardhiyyah, M. P., Izzah-Syafiah, M. A., Muhd-Farouk, H., Manan, H., Mahsol, H. H., Nadirah, M., & Ikhwanuddin, M. (2019). Dataset on reproductive status of ovary mud crab at different salinity levels. *Data in Brief*, *26*, 104426. https://doi.org/10.1016/j.dib.2019.104426

Han, W., Liu, H., & Wang, Y. (2024). Changes of nutrient composition in the ovaries and hepatopancreas of mud crab *Scylla paramamosain* broodstock and their offspring performance at different salinities. *Aquaculture*, *585*, 740704. https://doi.org/10.1016/j.aquaculture.2024.740704

Aaqillah-Amr, M. A., Hidir, A., Noordiyana, M. N., & Ikhwanuddin, M. (2018). Morphological, biochemical and histological analysis of mud crab ovary and hepatopancreas at different stages of development. *Animal Reproduction Science, 195,* 274–283. https://doi.org/10.1016/j.anireprosci.2018.06.005

Yu, K., Xu, H., Shi, C., Wang, C., Mu, C., Ye, Y., Chen, S., Li, R., & Wu, Q. (2025). Overwintering temperature affects lipid and fatty acid metabolism in hepatopancreas and ovary of female mud crab *Scylla paramamosain*. *Aquaculture Reports*, *40*, 102563. https://doi.org/10.1016/j.aqrep.2024.102563

Vo, H. D., Tran, N. T., & Fukuzawa, M. (2025). Experimental study on spectrometric features of mud crabs for automatic internal quality grading. In *Communications in Computer and Information Science* (Vol. 2191, pp. 3–14). Springer. https://doi.org/10.1007/978-981-97-9616-8_1

Tran, N. T., Vo, H. D., Ngo, C. T., Nguyen, Q. H., & Fukuzawa, M. (2024). Towards automatic internal quality grading of mud crabs: A preliminary study on spectrometric analysis. In *Communications in Computer and Information Science* (Vol. 1950, pp. 3–14). Springer. https://doi.org/10.1007/978-981-99-7666-9_1

Wold, J. P., O'Farrell, M., Tschudi, J., & Lorentzen, G. (2024). Rapid and non-destructive quantification of meat content in the legs of live red king crab (*Paralithodes camtschaticus*) by near-infrared spectroscopy. *LWT*, *201*, 116246. https://doi.org/10.1016/j.lwt.2024.116246

Moosavi-Nasab, M., Khoshnoudi-Nia, S., Azimifar, Z., & Kamyab, S. (2021). Evaluation of the total volatile basic nitrogen (TVB-N) content in fish fillets using hyperspectral imaging coupled with deep learning neural network and meta-analysis. *Scientific Reports*, *11*(1), 84659. https://doi.org/10.1038/s41598-021-84659-y

Kong, D., Shi, Y., Sun, D., Zhou, L., Zhang, W., Qiu, R., & He, Y. (2022). Hyperspectral imaging coupled with CNN: A powerful approach for quantitative identification of feather meal and fish by-product meal adulterated in marine fishmeal. *Microchemical Journal*, *180*, 107517. https://doi.org/10.1016/j.microc.2022.107517

Li, P., Tang, S., Chen, S., Tian, X., & Zhong, N. (2023). Hyperspectral imaging combined with convolutional neural network for accurately detecting adulteration in Atlantic salmon. *Food Control, 147,* 109573. https://doi.org/10.1016/j.foodcont.2022.109573

Shao, Y., Shi, Y., Wang, K., Li, F., Zhou, G., & Xuan, G. (2023). Detection of small yellow croaker freshness by hyperspectral imaging. *Journal of Food Composition and Analysis*, *115*, 104980. https://doi.org/10.1016/j.jfca.2022.104980

Zhang, H., Zhang, S., Chen, Y., Luo, W., Huang, Y., Tao, D., Zhan, B., & Liu, X. (2020). Non-destructive determination of fat and moisture contents in salmon (*Salmo salar*) fillets using near-infrared hyperspectral imaging coupled with spectral and textural features. *Journal of Food Composition and Analysis*, *92*, 103567. https://doi.org/10.1016/j.jfca.2020.103567

Ismail, A., Yim, D. G., Kim, G., & Jo, C. (2023). Hyperspectral imaging coupled with multivariate analyses for efficient prediction of chemical, biological and physical properties of seafood products. *Food Engineering Reviews*, *15*(1), 41–55. https://doi.org/10.1007/s12393-022-09327-x